Analysis of quantitative biomarkers from longitudinal MR imaging of cancer patients

C. Tresch

June 2025

Abstract

This project aimed to investigate correlations between local treatment failure and radiomics features derived form pre-treatment apparent diffusion coefficient distributions within the gross tumor volume. A cohort of 11 brain tumor patients, 3 of whom exhibited local treatment failure, was retrospectively analyzed. For each patient 58 radiomics features were extracted from normalized apparent diffusion coefficient maps registered to planning computed tomography images on which segmentation had been performed with either rigid or affine registration. For each extracted feature f and registration modality m its Spearman rank correlation coefficient ρ_f^m with local treatment failure as well as the associated p-value p_f^m was calculated. Of the considered features only sphericity correlated significantly with local treatment failure, with $\rho^{\mathrm{r,a}}_{\mathrm{Sphericity}} = 0.65$ and $p^{\mathrm{r,a}}_{\mathrm{Sphericity}} = 0.049$. A number of other features related to intensity heterogeneity were found to correlate moderately with local treatment failure, however without reaching the significance threshold of $p_f^m < 0.05$.

1 Introduction

According to the World Health Organization as of 2018 cancer accounted for 1 in 6 deaths globally, with numbers projected to rise further over the coming decades [1]. Consequently the prevention, diagnosis and treatment of cancer is a prolific area of research within the medical field and beyond. Among the various treatment approaches in use today, Radiotherapy (RT) is one of the most significant, with approximately half of all cancer patients requiring RT at least once during their treatment [2, 3]. RT utilizes well-localized high doses of radiation to cause irreversible damage to cancer cells, inhibiting their spread. While conventional RT delivers dose through x-ray photons, an increasing number of patients are being treated with particle therapy (PT), where dose is instead delivered by heavy particles, most commonly protons. Since heavy particles deposit their dose more locally than photons, PT has the potential to reduce radiation dose to healthy tissue, which may lower the risk of radiation-induced adverse side effects [4, 5, 6]. PT's dose deposition properties emphasize the need for high precision and accuracy of dose delivery, which can be achieved by image guidance [7]. Medical imaging is a critical component in any RT (and PT in particular) workflow and at all stages of the process, from diagnosis to treatment planning and outcome assessment. Currently the most prevalent imaging technique used in RT is Computed Tomography (CT), as CT scans provide both high-resolution anatomical images used for segmentation and information on density distribution within tissues necessary for dose calculations. However, CT has certain limitations, namely its

poor soft tissue contrast and the absence of functional information. Consequently there have been efforts to assess the viability of other imaging modalities in addressing these limitations [8, 9, 10]. Among others, Diffusion-Weighted Imaging (DWI) has gained attention as a functional imaging technique that has shown promise in a wide range of applications in RT, such as improving pre-treatment outcome prediction, tumor delineation and post-treatment response assessment [11, 12, 13]. DWI is an MR-based imaging technique, which uses two pulsed field gradients to sensitize the measurement to diffusion. The first gradient pulse dephases proton spins, whereafter the second pulse rephase them. If no diffusion occurred between the two gradient pulses, spins will be rephased precisely, resulting in no signal loss, while areas of high diffusion will have significantly reduced signal due to imperfect rephasing. The ratio between the signal $S(TE)$ with diffusion-sensitizing gradients and the S_0 without can be calculated as

$$\frac{S(TE)}{S_0} = \exp\left[-\gamma^2 G^2 \delta^2 (\Delta - \frac{\delta}{3}) D\right] \tag{1}$$

where γ is the gyromagnetic ratio, G is the diffusion sensitizing pulse's strength and δ is its duration, Δ is the time between the dephasing and rephasing pulse and D is the diffusion coefficient [14]. The loss in signal is however complicated by the presence of the gradient fields used for signal localization in MRI, leading to deviations from the behavior predicted by Equation 1. Hence a simplified relation for $S(TE)/S_0$ has been proposed [15]:

$$\frac{S(TE)}{S_0} = \exp\left(-b \cdot ADC\right) \tag{2}$$

The b-factor summarizes the the effect of all gradient fields, controls the strength of diffusion weighting and is dependent on user-controlled acquisition parameters. By acquiring diffusion-weighted images at various values of b ADC maps can be calculated. From such maps a large number of quantitative metrics, so-called radiomics features, may be extracted to assess a variety of tissue characteristics. This radiomics-based approach to DWI has shown promise in predicting histologic grade of tumors and treatment outcome for a variety of treatment approaches and tumor types [16, 17, 18, 19, 20]. This study specifically aims to investigate potential correlations of radiomics features extracted form pre-treatment ADC maps and local treatment failure after proton therapy, with the goal of identifying features that may serve as predictors of treatment outcome.

2 Methods

The study was retrospectively performed on a cohort of 11 brain tumor patients treated with proton therapy. Of the 11 patients 3 experienced local treatment failure. For each patient a pre-treatment ADC map, a T1-weighted MR image, a planning CT and a contour file with various segmented regions of interest (ROI), among which the gross tumor volume (GTV), were utilized for this study.

2.1 Image Registration

Since planning CT images on which segmentation was performed and ADC maps were acquired on different imaging systems and at different points in time image registration was necessary before any further analysis could take place. The SimpleITK Python package was used to implement a registration pipeline [21]. Due to the dissimilarity of ADC and CT

images, direct registration of the two was not feasible. Instead the registration process was split into multiple stages, first registering ADC to T1 and subsequently registering T1 to CT. The spatial transforms calculated in the two stages could then be concatenated to achieve registration of ADC to CT.

Like other optimization problems, successful registration is dependent on the choice of an appropriate initial guess. To obtain adequate initial estimates, brain masks were extracted from the ADC, T1 and CT images and aligned. In the case of the CT and T1 image brain masks were extracted using TotalSegmentator in Python [22]. To extract brain masks from the ADC maps, the latter were first normalized by defining a lower and upper cutoff value, (0.3 and 1.5) $\times 10^{-3}$mm^2/s respectively. The range between the cutoff values was then normalized to the interval $[0, 1]$ and subsequently values outside $[0, 1]$ were set the corresponding interval edges. The normalized maps were smoothed with a gaussian filter with $\sigma = 0.5$ and binary maps were then obtained by setting values below 0.4 to 0 and values above to 1. Brain masks were extracted by identifying the largest connected region within the binary maps and performing a 2-iteration binary closing on the region to eliminate small gaps in the mask. 18-connected neighborhoods were used both to for the extraction of the largest connected region and the binary closing operation.

Initial estimated for the T1-CT registration stage were obtained by converting the binary brain masks to signed distance fields (SDF) and subsequently registering these SDF. Due to the lower reliability of the extracted ADC brain masks initial guesses for the ADC-T1 registration stage were simply obtained by aligning the centers of mass of the ADC and T1 brain masks, using SimpleITK's CenteredTransformInitializer. These initial guesses were then used to set up to the respective registration methods for the T1-CT and ADC-T1 registration stages. The parameters used to set up individual registration methods are summarized in Table 1. Finally, the optimized transforms from both registration stages were concatenated and the ADC maps were resampled onto the corresponding planning CT images through linear interpolation.

Table 1: Table listing the relevant parameters used to set up registration methods applied at different stages of the registration pipeline.

Registration Stage	T1-CT brain mask SDFs	ADC-T1	T1-CT
Transformation Type	Euler3D		Euler3D/Affine
Initial Estimate	Moments-bases alignment of brain mask SDFs	Moments-based alignment of brain masks	Optimized alignment of brain mask SDFs
Similarity Metric	MeanSquares	MattesMutualInformation (numberOfHistogramBins = 32)	
Metric Fixed Mask	None	T1 brain mask	CT head mask
Optimizer	RegularStepGradientDescent (learningRate = 1.0, minStep = 1e-4, numberOfIterations = 200, gradientMagnitudeTolerance = 1e-6)		
Interpolator	linear		

2.2 Mask Creation

Since the available GTV segmentations contained an insuffcient number of points to directly reconstruct GTV masks additional segmentation points had to be artificially generated. This was done by first connecting contour points located on the same axial slice and subsequently resampling these axial contours to contain a fixed number of points per slice. Axial slices that contained no contour points were then populated by intersecting triangles generated through Delunay triangulation of the resampled contour points. After having populated all axial slices with contour points, masks could be created by generating polygons on each axial slice and defining regions within said polygons as within the mask.

2.3 Feature Extraction

Prior to feature extraction, two pre-processing steps were performed on the ADC maps, in order to account for inter-patient variability arising from differences in acquisition protocols and setups. In a first step all ADC maps were resampled to a common voxel spacing of $1\text{mm} \times 1\text{mm} \times 2\text{mm}$ using linear interpolation and GTV masks were subsequently resampled onto the resulting grids of the respective ADC maps. Secondly, ADC maps were normalized using z-score normalization. This approach has been shown to improve comparability of images for MR-based imaging techniques, including brain ADC maps [23]. The mean and standard deviation used for z-score normalization were calculated from the ADC distribution within the brain excluding the GTV, as ADC distributions within the GTV could not be assumed to be comparable between patients. Feature extraction from ADC maps within GTVs was then performed using the Pyradiomics Python package [24]. A fixed bin number approach with 128 bins was chosen for intensity discretization, as this approach was shown to yield better stability of radiomics features than a fixed bin size approach [25]. A total of 58 features were extracted for each patient, excluding directionally dependent features (features related to the Gray Level Co-occurrence Matrix and the Gray Level Run Length Matrix) as well as shape features not related to tumor volume or surface area.

2.4 Data Analysis

Non-normalized ADC distributions within the whole brain, the brain excluding the GTV and the GTV were extracted. This was done for both registration modalities. For each patient and both registration modalities a two-sample Kolmogorov-Smirnov test (KS-test) was conducted to assess the similarity of the ADC distributions within the GTV and the brain without GTV.

For each radiomics feature extracted from the resampled and normalized ADC maps its correlation with local failure was calculated. Spearman's rank correlation coefficient was used to this end, as no underlying distribution was assumed for the features and local failure, necessitating the use of non-parametric tests. Due to the small patient cohort considered in this project, p-values associated with the correlation coefficients were calculated by performing permutation tests with $n = 10000$ permutations each. 95% confidence intervals for the correlation coefficients were extracted from distributions generated through bootstrapping, with $n = 10000$ samples each. This analysis was performed both for ADC maps registered using rigid and affine registration for the T1-CT registration stage.

Additionally, the values of radiomics features obtained from rigid and affine registration were compared by calculating two-way mixed single score intraclass correlation coefficients (ICC3)

for each feature using the Pingouin python package [26].

3 Results

Figures 1-11 show the non-normalized ADC distributions within various ROI for each patient as obtained from rigid and affine registration of ADC maps. The KS-tests conducted to compare ADC distributions within the GTV and the brain without GTV yielded p-values of 0 for all patients and registration modalities, except for P0201, where p-values of 8×10^{-222} and 6×10^{-248} were found for rigid and affine registration respectively. Mean ADC across all patients was calculated to be $\mathrm{ADC}_{\mathrm{mean}}^{\mathrm{GTV}} = (1.5 \pm 0.7) \times 10^{-3} \mathrm{mm}^2/\mathrm{s}$ and $\mathrm{ADC}_{\mathrm{mean}}^{\mathrm{brainwoGTV}} = (1.0 \pm 0.5) \times 10^{-3} \mathrm{mm}^2/\mathrm{s}$ in the case of rigid registration and $\mathrm{ADC}_{\mathrm{mean}}^{\mathrm{GTV}} = (1.6 \pm 0.7) \times 10^{-3} \mathrm{mm}^2/\mathrm{s}$ and $\mathrm{ADC}_{\mathrm{mean}}^{\mathrm{brainwoGTV}} = (1.0 \pm 0.5) \times 10^{-3} \mathrm{mm}^2/\mathrm{s}$ in the case of affine registration. ICC3 scores for comparison of feature values derived from rigid and affine registration are shown in Figure 12. Figures 13 and 14 show the results from the correlation analysis of radiomics features and local failure as derived from both registration modalities.

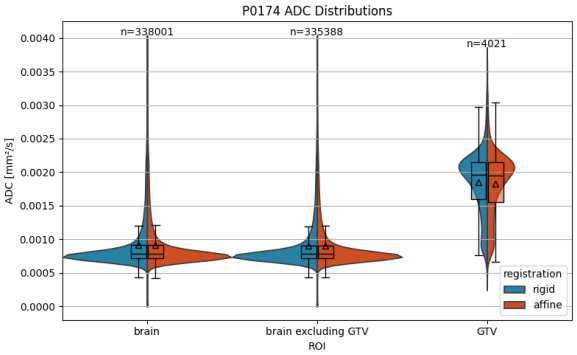

Figure 1: Figure showing ADC distributions in the whole brain, brain without GTV and GTV for patient P0174 as obtained by rigid and affine registration.

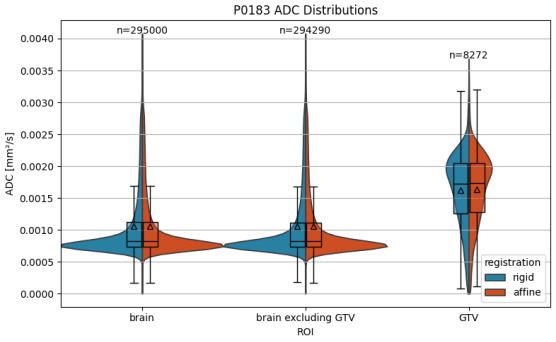

Figure 2: Figure showing ADC distributions in the whole brain, brain without GTV and GTV for patient P0183 as obtained by rigid and affine registration.

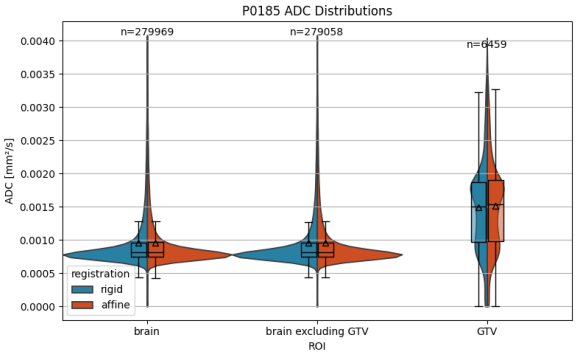

Figure 3: Figure showing ADC distributions in the whole brain, brain without GTV and GTV for patient P0185 as obtained by rigid and affine registration.

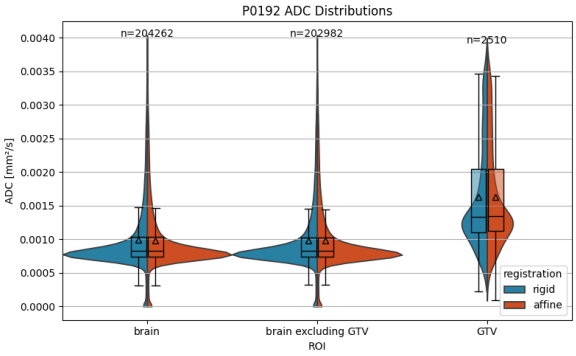

Figure 4: Figure showing ADC distributions in the whole brain, brain without GTV and GTV for patient P0192 as obtained by rigid and affine registration.

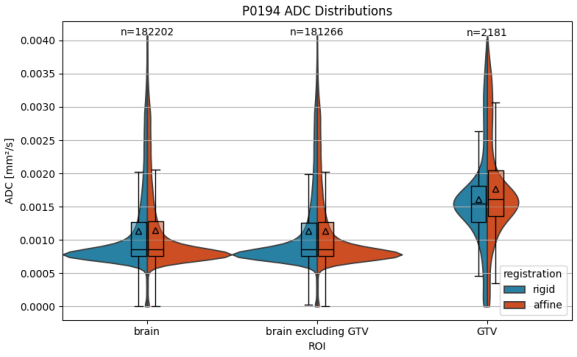

Figure 5: Figure showing ADC distributions in the whole brain, brain without GTV and GTV for patient P0194 as obtained by rigid and affine registration.

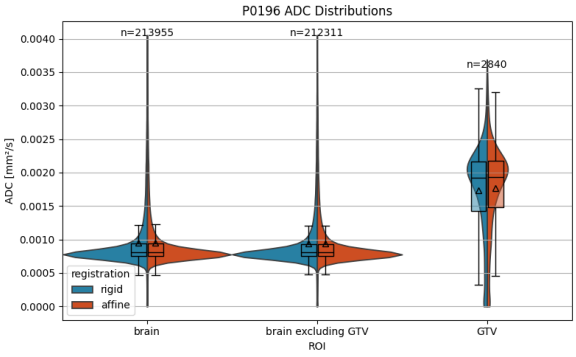

Figure 6: Figure showing ADC distributions in the whole brain, brain without GTV and GTV for patient P0196 as obtained by rigid and affine registration.

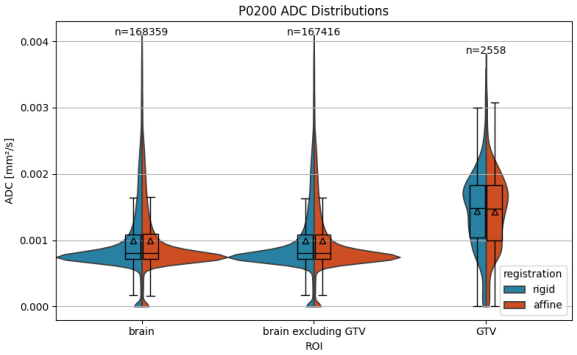

Figure 7: Figure showing ADC distributions in the whole brain, brain without GTV and GTV for patient P0200 as obtained by rigid and affine registration.

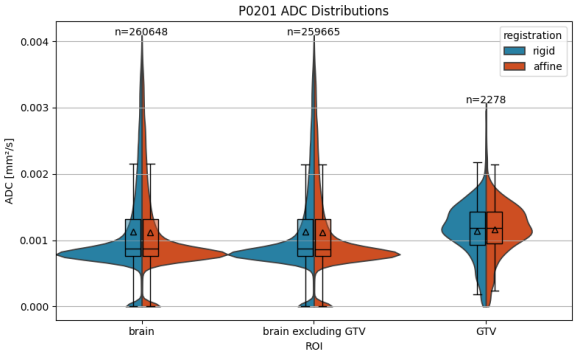

Figure 8: Figure showing ADC distributions in the whole brain, brain without GTV and GTV for patient P0174 as obtained by rigid and affine registration.

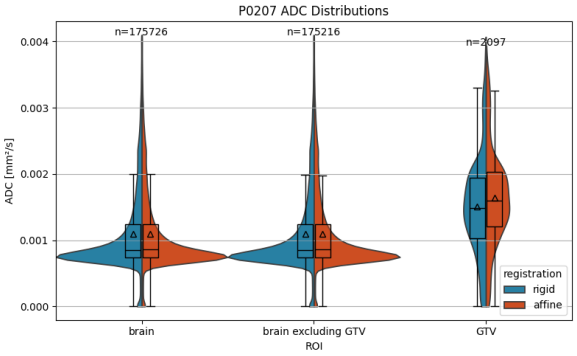

Figure 9: Figure showing ADC distributions in the whole brain, brain without GTV and GTV for patient P0207 as obtained by rigid and affine registration.

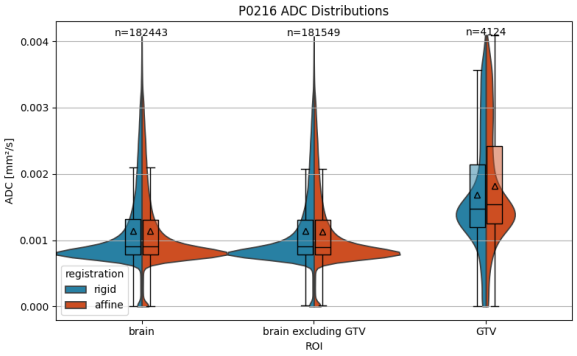

Figure 10: Figure showing ADC distributions in the whole brain, brain without GTV and GTV for patient P0216 as obtained by rigid and affine registration.

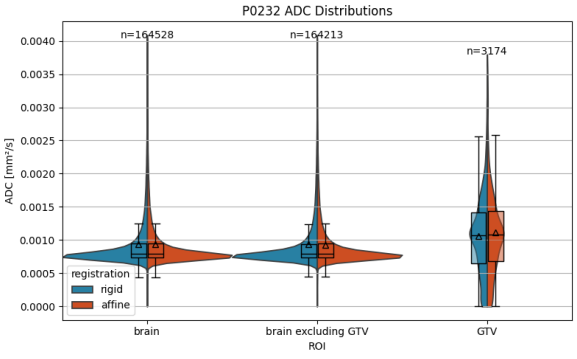

Figure 11: Figure showing ADC distributions in the whole brain, brain without GTV and GTV for patient P0232 as obtained by rigid and affine registration.

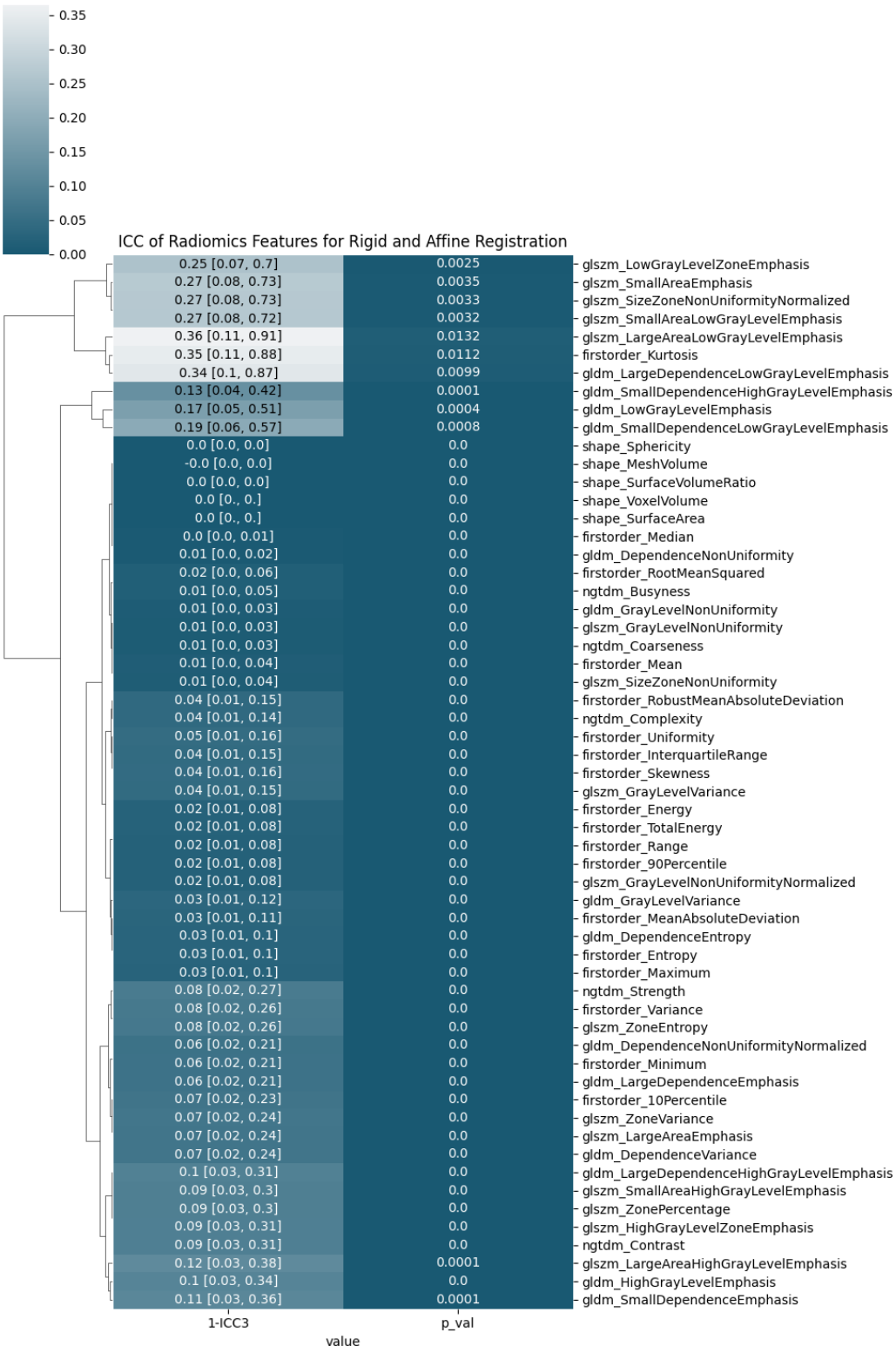

Figure 12: Figure showing ICC3 values, associated 95% confidence intervals and p-values for the 58 radiomics features.

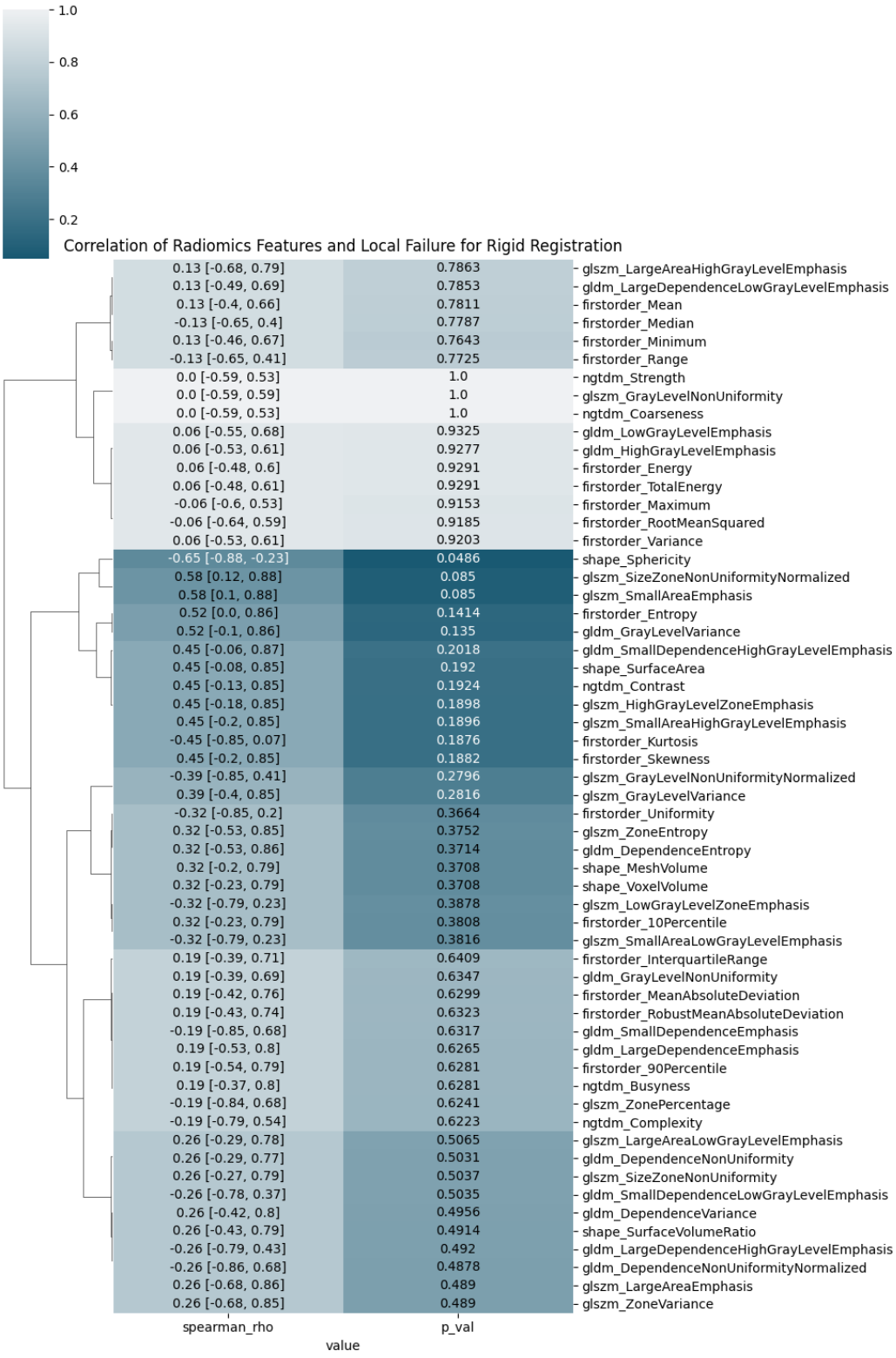

Figure 13: Figure showing Spearman's rank correlation coefficient of local failure and 58 radiomics features as derived from rigid registration of ADC maps. P-values associated with the correlation coefficients were calculated using permutation tests with 10000 permutations each, while 95% confidence intervals were extracted from 10000-sample distributions generated by bootstrapping.

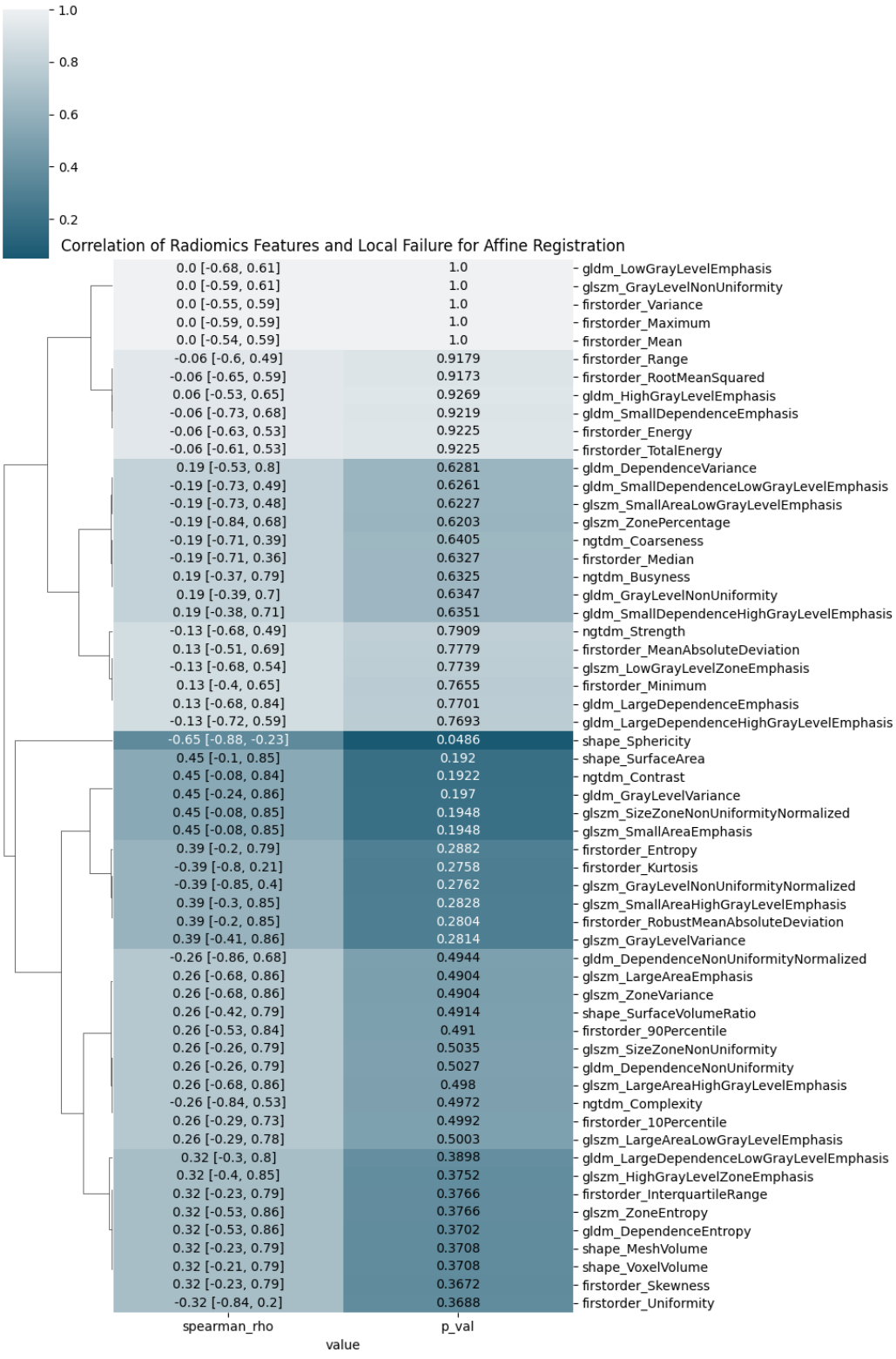

Figure 14: Figure showing Spearman's rank correlation coefficient of local failure and 58 radiomics features as derived from affine registration of ADC maps. P-values associated with the correlation coefficients were calculated using permutation tests with $n = 10000$ permutations each, while 95% confidence intervals were extracted from 10000-sample distributions generated by bootstrapping.

4 Discussion

It is apparent from Figures 1-11 and the results of the KS-tests that there is a significant difference between ADC distributions within the GTV and the surrounding brain. Comparing the ADC distributions found in this study to previously reported values proves difficult however, since previous studies most often discriminate tumors by type and pathological grade. Such distinctions were not feasible in this study, as data on tumor types and grades was not available. Additionally, measured ADC values have been shown to be dependent on acquisition parameters [27, 28]. Consequently, direct comparison of ADC distributions may inherently be of limited use. A more meaningful comparison might be achieved by using ADC ratios, computed by dividing tumor ADC by the mean ADC of a reference tissue, usually healthy white matter in the case of brain tumors. ADC ratios could however also not be calculated in this study, as no suitable segmented reference tissue was available. With due reservations it can however be said that our findings of mean ADC within tumor tissue agree with reported values of mean ADC in low grade tumors, specifically as reported by Hassannejad et al., who reported $\mathrm{ADC}_{\mathrm{mean}} = (1.5445 \pm 0.08131) \times 10^{-3}\mathrm{mm}^2/\mathrm{s}$ in Grade I adult brain tumors [29].

$\mathrm{ADC}_{\mathrm{mean}}$ measured in the brain without GTV yield significantly higher values than those reported by Helenius et al., who found whole-brain mean ADC values in healthy adults to be $\mathrm{ADC}_{\mathrm{mean}} = (0.89 \pm 0.04) \times 10^{-3}\mathrm{mm}^2/\mathrm{s}$. The elevated value found in this study may be attributed to the presence of tumor tissue outside the GTV, which may have skewed the measured $\mathrm{ADC}_{\mathrm{mean}}$.

Out of the 58 considered radiomics features 45 yielded very similar results between rigid and affine registration, reaching ICC > 0.9 and only 7 features fell below ICC < 0.75. As expected, shape features were identical for both registration methods, as they only depend on the ROI mask used for feature extraction. Of the 13 features with ICC < 0.9 12 were GrayLevelSizeZoneMatrix (GLSZM) and GrayLevelDependenceMatrix (GLDM) features. This agrees with findings by Traverso et al., who reported poor reproducibility of features related to image texture, such as GLSZM features, although their analysis did not not include GLDM features [30].

Among the considered features only shape_Sphericity reaches the significance threshold of $p < 0.05$, while correlating strongly ($|\rho| \geq 0.6$) with local failure with a correlation coefficient of $\rho_{\mathrm{Sphericity}} = 0.65$. It does so for both registration modalities as expected, since shape features are independent of intensity distributions. While no other features reach $p < 0.05$ there are a number of notable features that correlate moderately ($0.4 \leq |\rho| < 0.6$) with local failure and reach $p < 0.2$, such as glszm_SizeZoneNonUniformityNormalized, glszm_SmallAreaEmphasis and gldm_GrayLevelVariance. Notably all of these features quantify the spatial and distributional heterogeneity of intensity levels within the tumor, which seems to indicate that a more heterogeneous tumor may correlate with local treatment failure. A similar finding has been reported for the case of cervical cancer by Jajodia et al. [20], although the features found to correlate with treatment outcome in said study differ from the ones found to be of interest in this study. Another study by Bollen et al. aimed at improving outcome predictions for oropharyngeal carcinoma through integration of ADC-derived radiomics features similarly finds gldm_GrayLevelVariance to be significantly associated with locoregional control, with shape_Sphericity being narrowly above the significance margin [31].

Features calculated from rigidly registered ADC maps tend to exhibit weaker correlation and

lower p-values than in the case of affine registration. This is somewhat unexpected, since ICC calculations seem to indicate good agreement between the two registration methods. The discrepancy does however seem to be systematic, with both registration methods yielding a similar ordering of features in terms of correlation coefficients and p-values. They are thus in good agreement on which features may correlate to local treatment failure, while disagreeing on the strength and significance of said correlation.

This study has several limitations: First and foremost the small patient cohort with a strong imbalance with regard to treatment outcome, which limits the statistical significance of the results outlined above, as evidenced by the extremely large 95% confidence intervals and overall low p-values of correlation coefficients. Secondly, there are concerns regarding the reproducibility of these results. Radiomics features extracted from MRI-based images have been shown to be sensitive to the choice of acquisition parameters, segmentation, normalization approaches and intensity discretization [30, 25, 32, 33]. The lack of universally agreed upon standards for harmonization of MRI-based images means that the pre-processing methods utilized in this project may have reasonably been exchanged in favor of others, which may have led to different results. Lastly, the robustness of the image registration pipeline utilized for this project has not been thoroughly validated. Future studies on this topic may benefit from addressing the above mentioned limitations by being conducted on larger patient cohorts, incorporating and comparing alternate harmonization approaches and utilizing well-validated registration pipelines.

5 Conclusion

The project outlined in this report investigated correlations of local treatment failure and radiomics features extracted from pre-treatment ADC distributions within the GTV. A registration pipeline for rigid and affine registration of ADC maps to planning CTs was implemented. Radiomics features were extracted from harmonized ADC maps using reconstructed GTV masks and their correlation with local failure was calculated. Of the considered features only shape_Sphericity was found to correlate significantly with local treatment failure, while a number of features related to intensity level heterogeneity showed moderate correlation, but failed to pass the significance threshold. Feature values extracted from rigid and affine registration of ADC maps were found to agree well, with the exception of a few features related to image texture. It was also found that mean ADC within GTVs was significantly elevated when compared to the rest of the brain.

In spite of its many limitations, this project may be of use as a starting point for future studies on outcome prediction in RT by providing an exploratory reference for pre-treatment intra-tumor ADC-derived radiomics features correlated with treatment outcome.

Acknowledgments

I would like to thank my supervisor Dr. Giovanni Fattori for providing the template from which the image registration pipeline utilized for this project was built an my second supervisor, PhD Candidate Bastien Golomer, for implementing the mask creation algorithm that was used to generate the GTV masks. Most importantly, I would like to thank both of them for making this project possible in the first place and their tireless support throughout the

process.

References

[1] *WHO report on cancer: setting priorities, investing wisely and providing care for all.* Tech. rep. Geneva: World Health Organization, 2020.

[2] Hongcheng Zhu et al. "Global radiotherapy demands and corresponding radiotherapy-professional workforce requirements in 2022 and predicted to 2050: a population-based study". In: *The Lancet Global Health* (Dec. 2024). ISSN: 2214109X. DOI: 10.1016/S2214-109X(24)00355-3.

[3] Michael B. Barton et al. "Estimating the demand for radiotherapy from the evidence: A review of changes from 2003 to 2012". In: *Radiotherapy and Oncology* 112.1 (July 2014), pp. 140–144. ISSN: 18790887. DOI: 10.1016/j.radonc.2014.03.024.

[4] Radhe Mohan. *A review of proton therapy – Current status and future directions.* June 2022. DOI: 10.1002/pro6.1149.

[5] Renáta Kiss-Miki et al. "Proton or photon? Comparison of survival and toxicity of two radiotherapy modalities among pediatric brain cancer patients: A systematic review and meta-analysis". In: *PLoS ONE* 20.2 February (Feb. 2025). ISSN: 19326203. DOI: 10.1371/journal.pone.0318194.

[6] Zhe Chen et al. *Proton versus photon radiation therapy: A clinical review.* 2023. DOI: 10.3389/fonc.2023.1133909.

[7] Shelby A. Lane, Jason M. Slater and Gary Y. Yang. *Image-Guided Proton Therapy: A Comprehensive Review.* May 2023. DOI: 10.3390/cancers15092555.

[8] Gisele C. Pereira, Melanie Traughber and Raymond F. Muzic. *The role of imaging in radiation therapy planning: Past, present, and future.* 2014. DOI: 10.1155/2014/231090.

[9] H. Herrmann et al. *Image guidance: past and future of radiotherapy.* Dec. 2019. DOI: 10.1007/s00117-019-0573-y.

[10] Daniela Thorwarth and Ludvig Muren. *Imaging science and development in modern high-precision radiotherapy.* Oct. 2019. DOI: 10.1016/j.phro.2019.11.008.

[11] Sara Leibfarth et al. *Potentials and challenges of diffusion-weighted magnetic resonance imaging in radiotherapy.* Nov. 2018. DOI: 10.1016/j.ctro.2018.09.002.

[12] Elizabeth M. Charles-Edwards and Nandita M. De Souza. "Diffusion-weighted magnetic resonance imaging and its application to cancer". In: *Cancer Imaging* 6.1 (2006), pp. 135–143. ISSN: 14707330. DOI: 10.1102/1470-7330.2006.0021.

[13] Vinit Baliyan et al. "Diffusion weighted imaging: Technique and applications". In: *World Journal of Radiology* 8.9 (2016), p. 785. ISSN: 1949-8470. DOI: 10.4329/wjr.v8.i9.785.

[14] E. O. Stejskal and J. E. Tanner. "Spin diffusion measurements: Spin echoes in the presence of a time-dependent field gradient". In: *The Journal of Chemical Physics* 42.1 (1965), pp. 288–292. ISSN: 00219606. DOI: 10.1063/1.1695690.

[15] D Le Bihan and E Breton. "In vivo magnetic resonance imaging of diffusion". In: *C. R. Seances Acad. Sci., Ser. 2* 301.15 (1985), pp. 1109–1112.

[16] Marco Bologna et al. "Relevance of apparent diffusion coefficient features for a radiomics-based prediction of response to induction chemotherapy in sinonasal cancer". In: *NMR in Biomedicine* 35.4 (Apr. 2022). ISSN: 10991492. DOI: 10.1002/nbm.4265.

[17] Rile Nai et al. "Using apparent diffusion coefficient maps and radiomics to predict pathological grade in upper urinary tract urothelial carcinoma". In: *BMC Medical Imaging* 24.1 (Dec. 2024). ISSN: 14712342. DOI: 10.1186/s12880-024-01540-w.

[18] Byung Sup Kim et al. “Apparent Diffusion Coefficient as a Predictive Biomarker for Survival in Patients with Treatment-Naive Glioblastoma Using Quantitative Multiparametric Magnetic Resonance Profiling”. In: *World Neurosurgery* 122 (Feb. 2019), e812–e820. ISSN: 18788769. DOI: 10.1016/j.wneu.2018.10.151.

[19] Ichiro Yamada et al. “Texture analysis of apparent diffusion coefficient maps in cervical carcinoma: Correlation with histopathologic findings and prognosis”. In: *Radiology: Imaging Cancer* 2.3 (May 2020). ISSN: 2638616X. DOI: 10.1148/rycan.2020190085.

[20] Ankush Jajodia et al. “Combination of radiomics and machine learning with diffusion-weighted mr imaging for clinical outcome prognostication in cervical cancer”. In: *Tomography* 7.3 (Sept. 2021), pp. 344–357. ISSN: 2379139X. DOI: 10.3390/tomography7030031.

[21] Bradley C. Lowekamp et al. “The design of simpleITK”. In: *Frontiers in Neuroinformatics* 7.DEC (Dec. 2013). ISSN: 16625196. DOI: 10.3389/fninf.2013.00045.

[22] Jakob Wasserthal et al. “TotalSegmentator: Robust Segmentation of 104 Anatomic Structures in CT Images • Content codes”. In: *Radiology: Artificial Intelligence* 5.5 (2023). DOI: 10.5281/zenodo.6802613. URL: https://www.github.com/wasserth/TotalSegmentator.

[23] Savannah R. Duenweg et al. “Comparison of intensity normalization methods in prostate, brain, and breast cancer multi-parametric magnetic resonance imaging”. In: *Frontiers in Oncology* 15 (2025). ISSN: 2234943X. DOI: 10.3389/fonc.2025.1433444.

[24] Joost J.M. Van Griethuysen et al. “Computational radiomics system to decode the radiographic phenotype”. In: *Cancer Research* 77.21 (Nov. 2017), e104–e107. ISSN: 15387445. DOI: 10.1158/0008-5472.CAN-17-0339.

[25] Zahra Khodabakhshi et al. “Magnetic resonance imaging radiomic features stability in brain metastases: Impact of image preprocessing, image-, and feature-level harmonization”. In: *Physics and Imaging in Radiation Oncology* 30 (Apr. 2024). ISSN: 24056316. DOI: 10.1016/j.phro.2024.100585.

[26] Raphael Vallat et al. *Pingouin*. URL: https://github.com/raphaelvallat/pingouin/blob/main/README.rst.

[27] Jens Johansson et al. “Normal Brain and Brain Tumor ADC: Changes Resulting From Variation of Diffusion Time and/or Echo Time in Pulsed-Gradient Spin Echo Diffusion Imaging”. In: *Investigative Radiology* 59.10 (Oct. 2024), pp. 727–736. ISSN: 15360210. DOI: 10.1097/RLI.0000000000001081.

[28] Luca Fedeli et al. “On the dependence of quantitative diffusion-weighted imaging on scanner system characteristics and acquisition parameters: A large multicenter and multiparametric phantom study with unsupervised clustering analysis”. In: *Physica Medica* 85 (May 2021), pp. 98–106. ISSN: 1724191X. DOI: 10.1016/j.ejmp.2021.04.020.

[29] Ehsan Hassannejad et al. “Correlation of ADC values of adult brain tumors with the diagnosis and pathological grade: A cross-sectional multicenter study”. In: *Health Science Reports* 7.6 (June 2024). ISSN: 23988835. DOI: 10.1002/hsr2.2110.

[30] Alberto Traverso et al. “Stability of radiomic features of apparent diffusion coefficient (ADC) maps for locally advanced rectal cancer in response to image pre-processing”. In: *Physica Medica* 61 (May 2019), pp. 44–51. ISSN: 1724191X. DOI: 10.1016/j.ejmp.2019.04.009.

[31] Heleen Bollen et al. “Improving outcome prediction in oropharyngeal carcinoma through the integration of diffusion-weighted magnetic resonance imaging radiomics”. In: *Physics and Imaging in Radiation Oncology* 34 (Apr. 2025). ISSN: 24056316. DOI: 10.1016/j.phro.2025.100759.

[32] Arpita Dutta et al. “Robustness of magnetic resonance imaging and positron emission tomography radiomic features in prostate cancer: Impact on recurrence prediction after radiation therapy”. In: *Physics and Imaging in Radiation Oncology* 29 (Jan. 2024). ISSN: 24056316. DOI: 10.1016/j.phro.2023.100530.

[33] Jurgen Peerlings et al. “Stability of radiomics features in apparent diffusion coefficient maps from a multi-centre test-retest trial”. In: *Scientific Reports* 9.1 (Dec. 2019). ISSN: 20452322. DOI: 10.1038/s41598-019-41344-5.